Applied Materials Today 30 (2023) 101697

Contents lists available at ScienceDirect

Applied Materials Today

journal homepage: www.elsevier.com/locate/apmt

Microwave assisted preparation of $LiFePO_4$/C coated $LiMn_{1.6}Ni_{0.4}O_4$ for Li-ion batteries with superior electrochemical properties

F.A. Vásquez [a], N.C. Rosero-Navarro [b,*], R. Jalem [c,*], A. Miura [b], Y. Goto [d], Y. Tateyama [c], J.A. Calderón [a,*], K. Tadanaga [b]

[a] CIDEMAT, Universidad de Antioquia, Street 70 # 52 – 21, Medellín, Colombia
[b] Division of Applied Chemistry, Faculty of Engineering, Hokkaido University, Sapporo, Japan
[c] Center for Green Research on Energy and Environmental Materials, National Institute for Materials Science (NIMS), Tsukuba, Japan
[d] Department of Physics, Tokyo Metropolitan University, Hachioji, 192-0397, Japan

ARTICLE INFO

Keywords:
Lithium-ion battery
microwave chemistry
olivine-spinel synchrotron
high-temperature performance
DFT interface modelling

ABSTRACT

$LiMn_{1.6}Ni_{0.4}O_4$ (LMNO) spinel is a promising cobalt-free electrode for high potential applications. However, its chemical stability against electrolytes is relatively poor. Inorganic coatings have widely used to achieve superior chemical and electrochemical properties. A promising example is $LiFePO_4$/C (LFP/C) olivine coated LMNO spinel particles, in which olivine provides a high chemical stability. Chemical incompatibility between them during atmospheric synthesis conditions makes the process extremely challenging. Herein, we propose a simple and practical route to prepare LFP/C-coated LMNO using microwave irradiation. This process significantly improves the crystallographic order of the spinel structure and provides sufficient physical interaction between both materials while avoiding side reactions. Li-ion battery using LFP/C-coated LMNO electrode exhibits a higher discharge capacity at 25°C and 60°C than those of uncoated spinel. Moreover, cyclability (up to 500 cycles) at 25°C and C-rate capability performances at 60°C are superior in LFP/C-coated LMNO particles and not possible using uncoated spinel.

1. Introduction

Lithium-ion batteries are an essential component of a wide variety of electronic devices, which play a key role in modern life. High-potential cathodes, particularly those based on cobalt-free materials, have been actively studied to develop electronic devices with high energy density, along with safe and reliable operation. Spinel-structured cathodes such as $LiMn_{1.6}Ni_{0.4}O_4$ (LMNO) are promising alternatives, with a theoretical capacity of 146.7 mAh g^{-1} (700 Wh kg^{-1}, 4.7 V *vs.* Li^+/Li). Compared to spinel $LiMn_2O_4$ with non-doped Mn sites, the initial discharge capacity loss associated with Jahn−Teller distortion of Mn^{3+} ions and Mn dissolution into the electrolyte is significantly improved for the LMNO spinel, because its proportion of insoluble manganese in the +IV oxidation state is considerably higher than that in $LiMn_2O_4$ [1]. Despite this favorable property, the LMNO spinel alone cannot prevent the dissolution of its transition metal ions upon long-term battery cycling, leading to inevitable capacity fading. The decomposition of the electrolyte, particularly under high voltage and elevated temperature conditions, accelerates the dissolution of the spinel. Several alternatives to improve the chemical stability have been studied as for example protective coatings, lattice modification and lattice doping to impro structural stability. The structural stability can also be improved via increases of entropy introducing several transitions metal [2,3]. Development of polyanionic structures $NVPP_x$ substituting the anions PO_4^{3-} by $P_2O_7^{4-}$, substituting the cation V^{3+} by Na^+ or doping with Si and S have been reported to improve structural stability, diffusion rate and electronic conductivity of the active material [4–6]. Coatings based on inorganic or polymeric materials such as metal oxides, polyanionic compounds, and carbon layers have been applied on the surface of spinel particles to prevent their direct contact with the electrolyte and then reduce side reactions at the particle surface [7,8]. Coatings based on materials such as $LiPO_3$, $Li_4Ti_5O_{12}$, and $LiFePO_4$ (LFP) provide not only surface passivation, but also a Li^+ diffusion pathway with low charge-transfer resistance, which enhances the initial discharge capacity and cycle life [9–12]. LFP olivine is an excellent candidate as coating layer because its properties can be complementary to those of LMNO spinel. In particular, LFP olivine is more chemically stable against electrolytes than LMNO spinel, because oxygen atoms are covalently bonded to phosphorus

* Corresponding author.
E-mail addresses: rosero@eng.hokudai.ac.jp (N.C. Rosero-Navarro), JALEM.Randy@nims.go.jp (R. Jalem), andres.calderon@udea.edu.co (J.A. Calderón).

https://doi.org/10.1016/j.apmt.2022.101697
Received 23 August 2022; Received in revised form 6 November 2022; Accepted 13 November 2022
Available online 24 November 2022

instead of transition metals, improving the stability of the LFP olivine structure [13]. If the LFP olivine coating is sufficiently thin, the problems associated with a low electronic conductivity should be mitigated; otherwise, carbon-coated LFP olivine (LFP/C) provides a sufficiently electronic conductivity and stable electrochemical performance.

The development of LFP-coated LMNO spinel is extremely challenging, because of the incompatibility between the two materials under air or argon atmosphere when a heat treatment is applied. Under Ar-atmosphere the LMNO spinel can discomposes into rhombohedral layered rock salt ($Li_{0.8}Mn_{0.8}O_2$) and NiO, and under air atmosphere the LFP olivine can discomposes into $Li_3Fe_2(PO_4)_3$ and Fe_2O_3 [14–16]. To the best of our knowledge, two routes have been used to prepare LFP-coated LMNO particles (Fig. 1): (a) *in situ* coating deposition and (b) mechano-fusion dry processes [11,12]. The traditional *in situ* coating deposition process involves the deposition of the LFP precursor on LMNO particles and subsequent heat treatment. This process is difficult to implement [11] without affecting the integrity of each material, because the spinel requires oxidizing conditions to keep the Mn ions in their higher valence state and prevent the formation of secondary phases. On the other hand, olivine requires reducing conditions to prevent the oxidation of iron. Jang et al. [12] studied the *in situ* coating deposition of an LFP precursor on LMNO particles, through heat treatment steps at low temperatures (500–600°C) under reducing conditions. An LFP coating with a thickness of ~ 2 nm considerably improved the cycle life of LMNO; however, the initial discharge capacity was up to 20% lower than that of the pristine LMNO spinel. The authors hypothesized possible changes in the spinel structure or side reactions between spinel and olivine during heat treatment, but no clear evidence was obtained. On the other hand, Liu et al. [11] employed a mechano-fusion dry process to prepare LFP/C-coated LMNO, in which particles of both materials were used without any heat treatment. Although the interaction between the two types of particles was not discussed in detail, the LFP/C-coated LMNO spinel showed an enhanced cycle life, which was attributed to the successful adhesion between the two materials [11]. The low discharge region at high potential associated with the Ni^{4+}/Ni^{2+} and Mn^{4+}/Mn^{3+} reduction processes was attributed to the large amount of LFP/C phase (20 wt.%). In summary, both routes present limitations in achieving the desired electrochemical properties of the LMNO spinel. Thus, a thin LFP/C coating layer to prevent the side reactions between LMNO spinel and liquid electrolyte maintaining a high lithium diffusion rate is needed to achieve a high discharge capacity and stable cycle life .

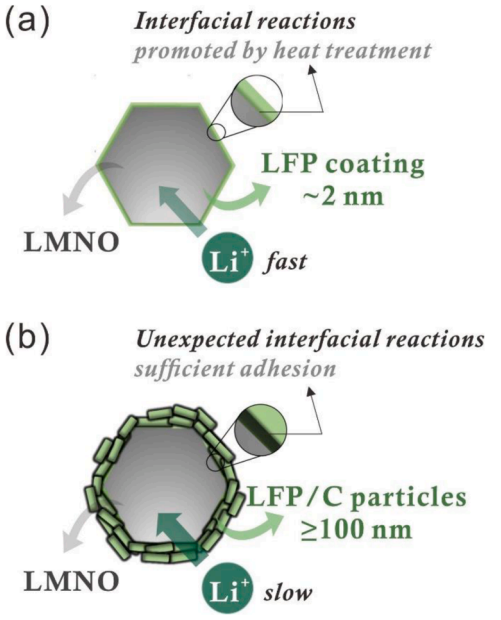

Fig. 1. Two-dimensional schemes of (a) LFP-coated LMNO preparation by in situ coating deposition and (b) preparation of LFP/C-coated LMNO by mechano-fusion dry process.

Processes involving microwave irradiation trigger a uniform and rapid heating through the energy absorption generated by electromagnetic waves directly on the particles. In particular, carbon provides significant advantages for microwave heating because of its high dielectric losses, which means that the microwave irradiation can lead to strong local heating and hot-spot formation (up to 1200°C at 1 kW for 1 min on 25 g) [17–20]. Evidence of enhanced adhesion of carbon to metal substrates such as nickel by microwave treatment has been reported by Su et al. [21]. In spite of the beneficial role of the LFP/C as protective coating for LNMO active material, as was mentioned above, little attention have been paid to the interface formed between LFP/C and LNMO phases, which can be the key to achieve better designs of the active composite material for lithium-ion batteries with superior electrochemical performance. According to knowledges of the authors there are not works concern about the interface formed between LFP/C and LNMO. Interfaces in lithium-ion batteries are important as reactive sites between the electrolyte and active electrode material and as pathways for lithium-ion intercalation. However, the methods for modelling interfaces in lithium-ion batteries reliably have been little developed [22]. According to Butler et al. [22] the interfacial properties are accessible by using modern electronic structure methods, particularly density functional theory (DFT).

In this work, we propose a simple and practical route to prepare an LFP/C-coated LMNO electrode using microwave irradiation in an organic solvent medium and the interface formed between LFP/C and LNMO is modeled by DFT calculations. The effect of the microwave irradiation is studied and compared with a simple mixture to rationalize their effect on physicochemical and electrochemical properties of the composite electrode. Electrochemical performance is evaluated at room temperature and extreme conditions of 60°C. The LFP/C-coated LMNO electrode obtained by microwave exhibits a higher discharge capacity, C-rate and thermal stability at 25°C and 60°C. The microwave absorption by the carbon layer on LFP particles is crucial to promote the adhesion between LFP/C and LMNO particles according to DFT interface calculations and provides an adequate interface to lithium intercalation between both phases and the electrolyte.

2. Results and discussions

Microwave heating approach of LFP/C olivine on LMNO spinel particles (LMNO-LFP/C) is illustrated in Fig. 2. We used LMNO and LFP/C particles in a weight ratio of 98:2 (the experimental details are provided in the Supporting Information). LMNO spinel particles (porous cluster) with sizes in the range of 10–30 μm containing secondary particles smaller than 2 μm were used (SEM images shown in Fig. 2). LFP/C nanoparticles with nanoplate morphology and dimensions of approximately 130 × 90 nm (TEM image in Fig. 2) were selected to be deposited as a layer on the LMNO particles, because their thickness can reach 10

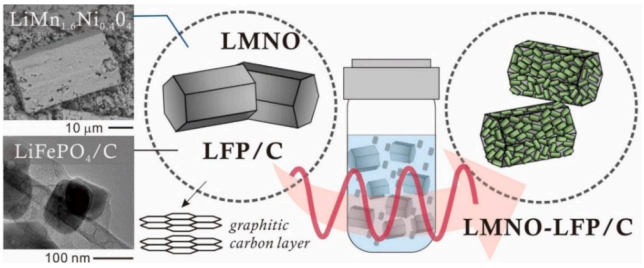

Fig. 2. Schematic illustration of the preparation of LMNO-LFP/C by microwave irradiation, including SEM and TEM images showing the morphology of the initial LMNO and LFP/C particles, respectively.

nm (with a 3-nm graphitic carbon layer), making them an ideal alternative to allow sufficient lithium diffusion to LMNO. Both the LMNO and LFP/C particles were dispersed in N-methylpyrrolidone solvent to facilitate their interaction, and microwave irradiation powers of 10 and 100 W (at 200 and 300°C, respectively) were evaluated. The overall microwave process took approximately 7 min, with almost negligible effect on the solvent used to perform the procedure (Fig. S1). After microwave heating, the material was washed and centrifuged with ethanol/water and dried at 80°C for 24 h. The LMNO-LFP/C samples were named according to the irradiation power employed, i.e., LMNO-LFP/C-10W and LMNO-LFP/C-100W. The pristine LMNO spinel irradiated at 10 W and the LMNO-LFP/C samples prepared by stirring with the same solvent were used as reference materials and named LMNO-10W and LMNO-LFP/C-S, respectively.

Fig.s S3 and S5 show SEM images of pristine LMNO spinel, LMNO-10W, and LMNO-LFP/C-10W. The morphology of LMNO-LFP/C-10W, with particle sizes between 5 and 20 μm, is similar to that observed for the pristine LMNO spinel or the sample irradiated at 10 W, but with a smooth surface. The morphology of the LMNO-10W particles suggests that the microwave process may promote exfoliation of the secondary particles. The smooth surface of the LMNO-LFP/C-10W particles is associated with the deposition of LFP/C nanoparticles, as confirmed by

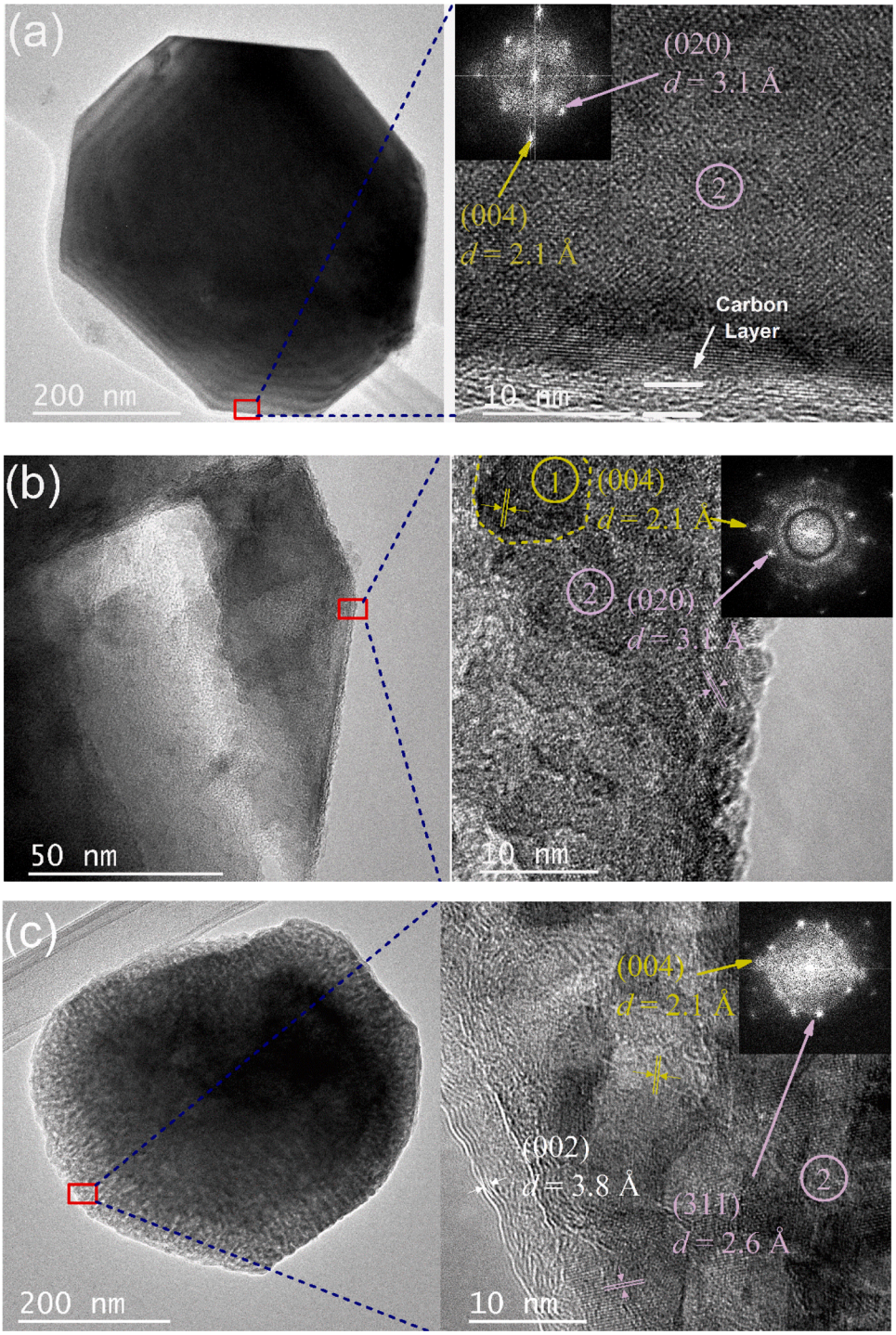

Fig. 3. (a–c) TEM images of LMNO-2LFP/C-10W showing the distribution of spinel and olivine phases.

the energy-dispersive spectroscopy (EDS) mapping in Fig. S5, in which the LFP olivine (Fe and P elements) is uniformly distributed on the LMNO spinel particles (Ni and Mn elements). At higher irradiation power, the morphology of LMNO-LFP/C-100W (not shown) is similar to that obtained using an irradiation powder of 10 W.

The TEM analysis of LMNO-LFP/C-10W is shown in Fig. 3. Each magnified TEM image includes the fast Fourier transform (FFT, inset) image obtained by the Gatan software [23,24]. The identification of LFP/C on LMNO is complicated because of the rather small size of the LFP/C nanoparticles (Fig. 2); therefore, the TEM analysis was performed on small LMNO particles. The presence of both phases is indicated by the change in contrast in the TEM image (plane orientation in the magnified images of Fig. 3a–c) between the planes assigned to LMNO spinel (region marked as 1) and the overlapping planes of both LFP olivine and LMNO spinel (region marked as 2). Further, both phases were confirmed by the FFT analysis, in which the *d*-spacing of 2.1 Å is assigned to the (004)

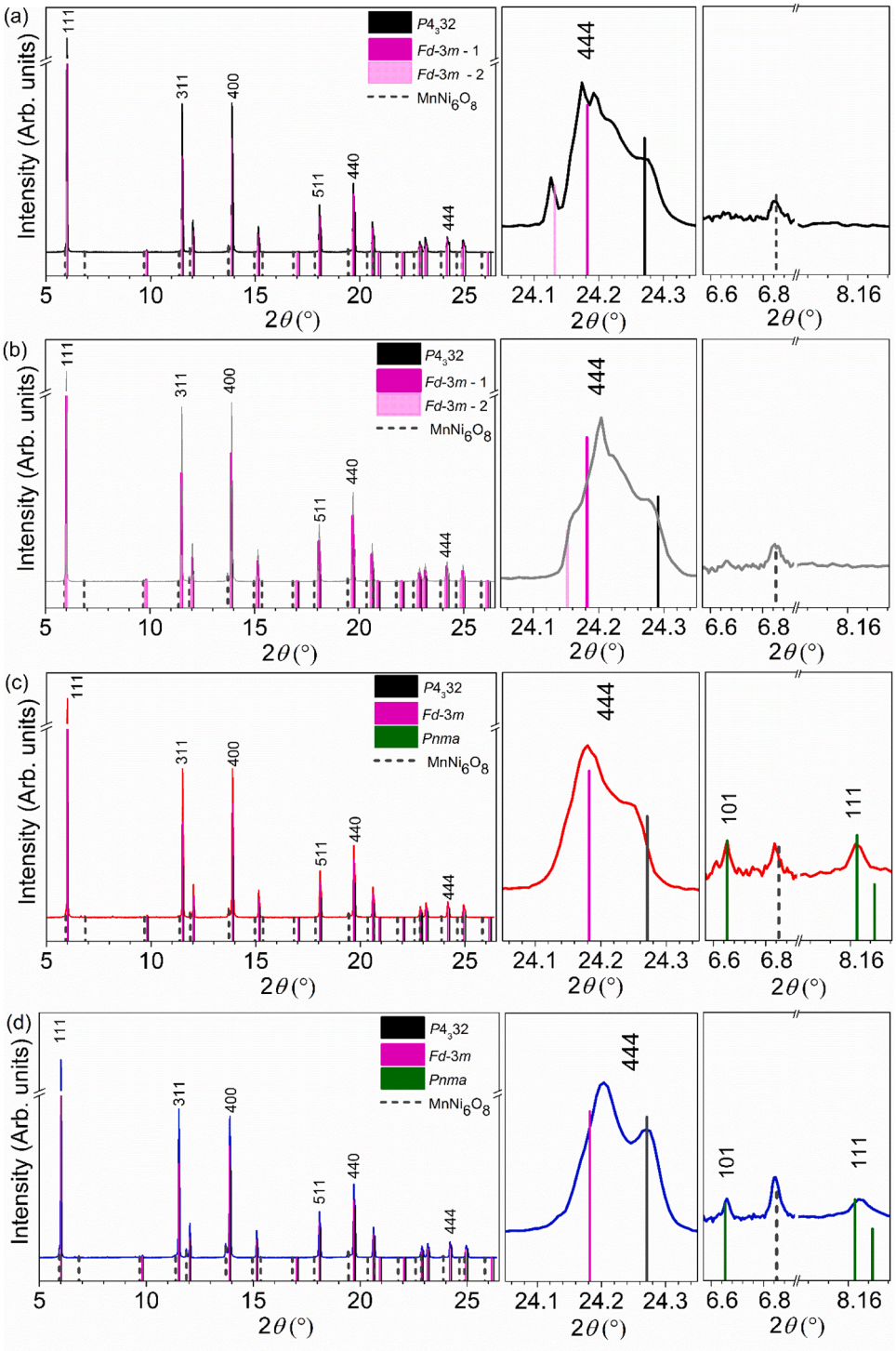

Fig. 4. Synchrotron XRD patterns obtained with a wavelength of 0.496197 Å (see Rietveld profiles in Fig. S7). (a) Pristine LMNO spinel, (b) LMNO-10W, (c) LMNO-LFP/C-10W, (d) LMNO-LFP/C-100W. The different colored lines denote the spinel (pink and black) and olive (dark green) phases. The signals of the secondary $MnNi_6O_8$ phase are also included.

plane of the LMNO spinel phase (see Fig. 3a-c), while the *d*-spacing values of 2.6 Å (Fig. 3c) and 3.1 Å (Fig. 3a-c) are assigned to the (311) and (020) planes of the LFP olivine phase, respectively. The presence of carbon between LMNO and LFP could not be confirmed, because of the overlap between the olivine and spinel planes; however, carbon was confirmed to be present in some of the spinel particles. In Fig. 3a, the layer of approximately 3 nm on the top of the particle is assigned to amorphous carbon, while the undulating planes with a *d*-spacing of 3.8 Å in Fig. 3c are assigned to the (002) plane of graphitic carbon [25]. Both the graphitic and amorphous carbon signals are attributed to the carbon coating on the olivine particles. The XPS profile of the LMNO-LFP/C-10W particles (Fig. S6) confirms the presence of the olivine and spinel phases, as well as carbon from LFP/C nanoparticles. Interestingly, the intense C–O bonds in the XPS profiles could be associated with the binding of LFP/C and LMNO particles. Overall, the SEM, TEM, and XPS analyses suggest that the two phases were closely linked; further details on the interaction between LFP/C and LMNO will be discussed later, bases on their electrochemical performance in Li-ion batteries and DFT interface modelling.

The synchrotron XRD patterns of pristine LMNO and LMNO-10W compared to those of the LMNO-LFP/C-10W and LMNO-LFP/C-100W samples is shown in Fig. 4. The figure includes two enlarged views of the regions corresponding to the LMNO spinel (444) and LFP olivine (101, 111) diffraction planes, respectively. The XRD fitting results are reported in Table S1 of the Supporting Information. The synchrotron XRD patterns of the pristine LMNO and LMNO-10W samples show the formation of a cubic spinel phase with various lattice parameters, including Ni-Mn cation order/disorder structures with spatial groups $P4_332$ (ICSD 98-009-8360) and $Fd\bar{3}m$ (ICSD 98-008-5399 and 98-009-4340) (Table S1, Fig. S7) [26–28]. The variation of the lattice parameters in the spinel phase is attributed to local changes in oxygen deficiency in this structure. In addition, a $MnNi_6O_8$ (ICSD 98-004-0584) [29] secondary phase was also identified. On the other hand, the synchrotron XRD patterns of LMNO-LFP/C-10W and LMNO-LFP/C-100W show the presence of the cubic spinel phase and additional peaks attributed to the orthorhombic olivine phase (magnified XRD, Fig. 4) with spatial group *Pnma* (ICSD 98-015-5580) [30,31]. The lattice parameter of the olivine phase in the LMNO-LFP/C material is in good agreement with those obtained for the pristine LFP/C sample (Fig. S8, Table S1).

Microwave heating does not seem to have a negative effect on the LMNO-LFP/C sample, because the absence of additional secondary phases suggests a negligible reaction between the two primary phases. Surprisingly, an important effect on the crystallinity of the LMNO spinel phase is observed in its enhanced crystallographic order. The effect of microwave irradiation is clearly shown by the split of diffraction peak (444) of the LMNO spinel (magnified XRD pattern, Fig. 4), which shows the presence of various lattice parameters, as mentioned above. This broad split peak also suggests the presence of residual strain (deformations) in the spinel crystal structure [32]. The residual strain was partially released after microwave irradiation of pristine LMNO spinel as can be observed in Fig. 4b and disappeared in LMNO-LFP/C samples with irradiation power of 10 and 100 W (see Fig. 4c-d) [33]. In those Figures no split of the diffraction peak (444) occurs. Microwave irradiation of the LMNO spinel produces a slight peak shift to higher angles (Fig. 4b), which is more evident in the LMNO-LFP/C samples (Fig. 4c,d), and is directly proportional to the irradiation power when it is increased from 10 to 100 W. Moreover, the peak shift is accompanied by a rather low residual strain in the spinel structure (narrow peaks), which denotes a high crystallographic order. The peak shift to higher angles indicates a spinel structure with small lattice parameters and a partial phase transformation from cation-disorder to cation-order structures (Table S1). This phase transformation can be the reason for the relatively high intensity of the peak associated with the $MnNi_6O_8$ phase ($2\theta = 6.8°$) in the LMNO-LFP/C-100W sample. The transition from cation order to cation disorder is controlled by the formation of oxygen vacancies and the corresponding changes in the Mn oxidation state, as described by the following equation: [33]

$$Li^+ + 0.5Ni^{2+} + 1.5Mn^{4+} + 4O^{2-} \underset{\rightarrow}{\leftarrow} Li^+ + 0.5Ni^{2+} + (1.5-2x)Mn^{4+} + 2xMn^{3+} + (4-x)O^2 \quad (1)$$

The electrochemical properties of the LMNO-LFP/C samples were evaluated as positive cathode electrodes of Li-ion battery cells at 25°C and 60°C, using 1.2 M $LiPF_6$ in ethylene carbonate and dimethyl carbonate (EC/DMC, 1:2 wt.%) as electrolyte and lithium metal as anode (details of cells assembly at experimental section). Fig. 5a shows the initial discharge profile (second cycle) of LMNO-LFP/C-10W and LMNO-LFP/C-100W at 0.5 C. For comparison, the electrochemical performances of pristine LMNO and of the sample prepared by simple stirring (LMNO-LFP/C-S) are also included.

The discharge capacities of pristine LMNO, LMNO-LFP/C-10W, and LMNO-LFP/C-100W were 111, 115, and 79 mAh g^{-1}, respectively. The discharge profiles of the LMNO spinels show two plateaus (Ni^{4+}/Ni^{2+} and Mn^{4+}/Mn^{3+} redox couples), while those of the LMNO-LFP/C electrodes containing olivine phase display an additional plateau related to LFP olivine (Fe^{3+}/Fe^{2+} redox couple) at the same potential than pristine LFP/C (Fig. S9) [34,35]. The discharge capacity fraction for the Ni^{4+}/Ni^{2+} plateau reaches approximately 61% of the total discharge for all samples, except for the LMNO-LFP/C-100W one (49%); on the other hand, in the case of the LMNO-LFP/C electrodes the discharge fraction for the Fe^{3+}/Fe^{2+} plateau is less than 4% of the total discharge (Fig. S10a). The dramatic difference in the initial discharge capacities of the LMNO-LFP/C-10W and LMNO-LFP/C-100W samples (Fig. 5a) suggests that excessive microwave irradiation is not beneficial for LMNO particles; this finding is in good agreement with the XRD analysis, which identified a spinel structure with small lattice parameters and an electrochemically inactive $MnNi_6O_8$ phase [36,37] (Fig. 4d and Table S1). The electrochemical performance of the LMNO was also found to be highly susceptible to similar heat treatments such as the stirring at relatively low temperatures (200°C) or microwave irradiations with or in absence of carbon (Fig. S10a). It should be noted that LMNO-LFP without a carbon layer by microwave irradiation show also a low initial discharge capacity. The reason of this last, suggests also that carbon even at rather low concentrations is crucial to promote the adhesion between the two phases and to stablish a favorable interphase to facilitate the lithium-ion intercalation.

Fig. 5b shows the discharge cycling performances of the LMNO, LMNO-LFP/C-S, and LMNO-LFP/C-10W samples. The LMNO and LMNO-LFP/C-S samples show a slight increase in the discharge capacity in the first two cycles, due to the activation and wetting of the active material during the initial cycles, [38,39] after which the discharge capacity decreases monotonically. In contrast, the LMNO-LFP/C-10W sample shows an increase in discharge capacity from 111 to 118 mAh g^{-1} during the first cycles, and then, the discharge capacity is basically constant. The capacity increases take place as consequence of active material wettability improvement during initial cycles. After 100 cycles, the LMNO, LMNO-LFP/C-S, and LMNO-LFP/C-10W retain 94%, 89%, and 97% of the initial capacity, respectively (Fig. 5b). Interestingly, LMNO-LFP/C-S shows a high initial discharge capacity, suggesting that the LMNO spinel and LFP olivine phases are active; however, capacity fading occurs in this sample related with the lack of adhesion between the two phases or the inexistence of an adequate interface between the two active phases which promotes the lithium-ion intercalation.

The internal resistances of these cells were examined after cycling (100 cycles) by impedance measurement at 50% state of charge-SOC (Fig. S11, Table S2). The internal cell resistances of LMNO and LMNO-LFP/C-10W are similar, while the one using LMNO-LFP/C-S is much higher (see Fig. S11b), in good agreement with the severe capacity fade observed in this electrode. The high internal resistance of the battery based on LMNO-LFP/C-S is attributed to the low electronic conductivity through the electrode due to the poor adhesion between the spinel and

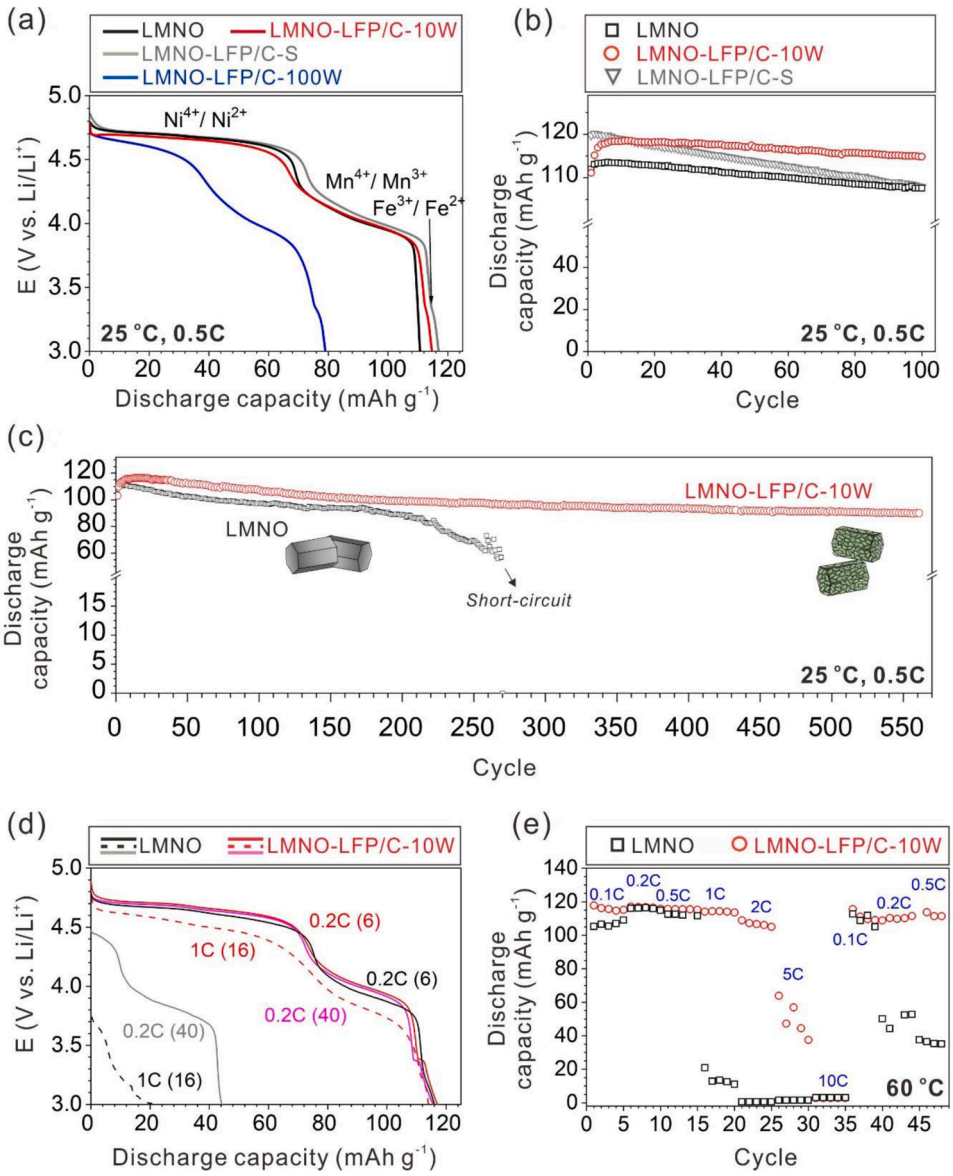

Fig. 5. (a) Discharge profiles (second cycle) and (b) cycling of LMNO, LMNO-LFP/C-S, LMNO-LFP/C-10W, and LMNO-LFP/C-100W operated at 25°C and 0.5C. (c) Long-term cycling of LMNO and LMNO-LFP/C-10W composite operated at 25°C and 0.5C. (d) Discharge profiles at 60°C (e) C-rate discharge capabilities of pristine LMNO and LMNO-LFP/C-10W at 60°.

olivine particles. The LMNO and LMNO-LFP/C-10W were also examined by synchrotron XRD (Fig. S12, Table S3) to understand the impact of the electrochemical performance on their crystal structures. For instance, the spinel structure of LMNO-LFP/C-10W remains almost unchanged, while LMNO shows a change in its crystallization order (peak 444 at lowest angles disappear) attributed to the partial dissolution of the manganese (details at supporting information in Fig. S12). Most significantly, the LMNO electrode shows the presence of Li_2CO_3 secondary phase which confirms its degradation after cycling [8,13]. The Li_2CO_3 phase is almost negligible in the LMNO-LFP/C-10W case.

The LMNO-LFP/C-10W shows a clear enhancement of the electrochemical stability than pristine LMNO at long-term cycling at 25°C, Fig. 5c. The pristine LMNO shows a severe capacity fading after 180 cycles and is short-circuited after 250 cycles. In contrast, the capacity of LMNO-LFP/C-10W became rather stable after 200 cycles and retain a high capacity of more than 90 mAh g^{-1} even after 550 cycles. These results and the low presence of Li_2CO_3 on the LMNO-LFP/C-10W cathode after 100 cycles (See Fig. S12) clearly suggest that the LFP/C coating reduces the interaction between the spinel and the electrolyte lessening the lixiviation of Mn and Ni from LMNO spinel into the liquid electrolyte. It seems also that the LFP/C coating reduces the possibility of dendrite formation on the anode material derived of Ni and Mn precipitation, as was described by T. Yi et al., and C. Birkl et al. [40,41]. The coulombic efficiency shows values of 75% and 88% in the first cycle for LMNO and LMNO-LFP/C-10W, respectively (see Fig. S10e), suggesting that a higher lithium amount can be consumed by the solid electrolyte interphase formation in the pristine LMNO than in the composite. The coulombic efficiency stabilization shows values of 99.1 and 98.2 for pristine LMNO and the composite, respectively. However, pristine LMNO material shows a progressive reduction of coulombic efficiency after 180 cycles, suggesting that the charge is consume by short-circuit.

The Figs. 5d and 5e show discharge profiles and C-rate at 60°C of LMNO and LMNO-LFP/C-10W. LMNO-LFP/C-10W shows an enhanced electrochemical performance at 60°C than pristine LMNO. The C-rate at 60°C shows higher performance for composite LMNO-LFP/C-10W retaining more than 90% at C-rates of 2C, higher than the pristine LMNO in which a discharge capacity is practically negligible. The capacity recovering of LMNO-LFP/C-10W at 0.1-0.5C, after 10C, is higher

than LMNO. Note that LMNO seems to achieve a comparable capacity to those of LMNO-LFP/C-10W but, in subsequent cycles, the capacity dramatically fades as a consequence of accelerated degradation. The enhanced C-rate performance at 60°C for composite LMNO-LFP/C-10W than LMNO (Fig. 5d) is attributed to the improvement of Li-ion diffusion (mobility) at higher temperatures, particularly those related to the olivine particles. In fact, the C-rate at 25°C (Fig. S10b-d) shows that the capacity at 10C of LMNO-LFP/C-10W is slightly lower than LMNO, probably because of the lower diffusion coefficient of the LFP/C olivine that lessen the C-rate performance for pristine LFP/C (Fig. S9c) and in accordance with their determined diffusivity values (Table S2). [42,43]. Nevertheless, the capacity recovery after high C-rate is again higher in LMNO-LFP/C-10W, which confirms the observations of the cell performances at 60°C. This means that the LMNO spinel coated with LFP/C retains a superior cycling and C-rate capability at room and high temperatures, achieving a rather high electrochemical performance than uncoated spinel. A slight attenuation of the LMNO capacity can be observed at 25°C because the presence of the LFP/C coating. This behavior could be probably due the lower diffusion coefficient of the olivine phase respect to spinel phase. However, the initial capacity attenuation problem is compensated by the better electrochemical behavior of the coated LMNO observed at high C-rate, high cycle numbers and high temperature tests.

The LMNO|LFP/C interface, promoted by microwave irradiation, was modeled with DFT calculations to gain a deeper understanding of the nature of the interaction strength between them that makes its superior electrochemical performance possible. The model is based on two considerations: (i) the LFP|C interface has a well-known and proven adhesion between C and LFP reflected in its improved electronic conductivity compared to bare LFP particles and, (ii) the adhesion between LMNO and LFP/C may occur at LMNO|C interface in which the carbon should absorb microwaves to promote it. Therefore, we studied the interaction strength between LMNO substrate and C via explicit interface structure modeling with DFT calculations (details at supporting information, Fig. S13-S14).

The result of the Bayesian-driven interface structure search (See supporting information, Sec.2.3) for the LMNO(100)|C(001) system is shown in Fig. 6a. Starting from an initial dataset size of 4 randomly picked interface slabs, the minimum DFT total-energy (E) structure (with geometry optimization) was quickly found by the algorithm at sampling step t = 1 (see Fig. 6b-c for the actual optimized structure and its optimized vertical shift at the contact region). Additional rounds of sampling with geometry optimization of candidate interface structures, such as at t = {2, 3, 4}, have resulted to slightly higher E values. Moreover, with further sampling at t = 5, the DFT-optimized slab structure resulted to an even higher E value. This structure search efficiency can be explained by the high symmetry of the two slabs (spinel and (001) hexagonal lattice points), which results to a highly periodic/repetitive slab-to-slab atom-stacking alignment in the lateral-shift direction (Fig. 6d). Meanwhile, the underlying probabilistic model (i.e., Gaussian process) has fairly deduced at t = 5 on which interface structures have high and low E values within the pre-defined sampling grid. This is made evident by the distinct overall shape of the evolved E landscape (Fig. S15), in which the predicted high (deep red) and low E (deep blue) regions are already clearly distinguishable at t = 5. Moreover, the prediction uncertainty on E is noted to be significantly reduced as well (see Fig. S16), as evidenced by the largely increased region with low DFT total-energy variance (σ^2) (i.e., increased blue color area at t = 5). Based on this level of confidence by the probabilistic model on the overall shape of the E landscape, including the sudden increase of E value at t = 5, the likelihood for finding other low-E interface structures is expected to be largely diminished at t > 5. Thus, the structure sampling procedure was terminated at t = 5.

The optimized vertical shift distance between the two slab materials was determined to be z = 2.764 Å, this value is comparable with those found in related oxide substrates with adsorbed graphene layers (Table S6). The interaction strength (binding energy, E_b) between LMNO (100) and C(001) was estimated to be -0.065 eV which indicates that the C(001) bilayer energetically prefers to be adsorbed on the LMNO(100) surface. However, the layer-decomposed DOS profiles (C-2s, C-2p states) for the graphene contact layer and graphene top layer do not show any significant electronic band perturbation (Fig. 7a, 6b). This suggests that no new chemical bonds are formed between C(001) contact layer and the exposed cations/anions on LMNO(100). In the LMNO(100) side, layer-by-layer DOS profiles (Fig. 7c-e) also show close similarity, with the Fermi level region dominated by O-2p states and the overall electronic structures of Mn and Ni closely resembling that of +4 ($t_{2g}^3e_g^0$) and +2 ($t_{2g}^6e_g^2$) oxidation states, respectively. Given these findings, the interaction between LMNO and C is thus determined to be physical adsorption. Collectively, the Mn/Ni-O bonding network from the LMNO bulk to its surface region, the adhesion of C on LMNO surface promoted by microwave irradiation, and the adhesion of C on the LFP particle surface are expected to enable electronic conduction and good particle contact in the LFP/C-coated LMNO composite cathode.

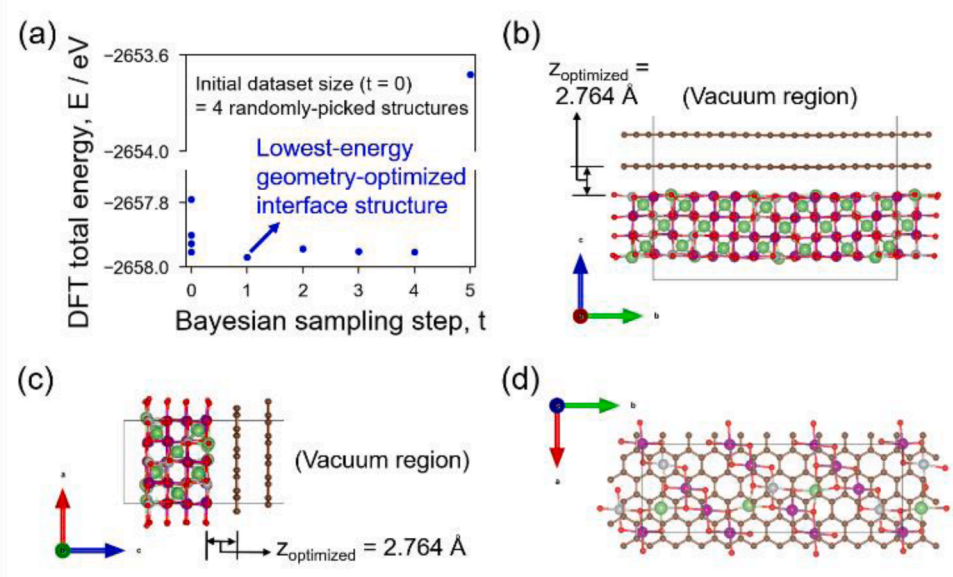

Fig. 6. (a) Interface structure sampling results for the LMNO(100)|C(001) by Bayesian-driven DFT-geometry optimization scheme. The lowest energy interface structure was found at sampling step t = 1. (b-c) Actual lowest-energy geometry-optimized interface structure (bc- and ac-plane view) showing the optimized vertical shift ($z_{optimized}$) at the contact region in the slab-normal direction. (d) Highlighted interface-slab contact region, showing only the C(001) bottom layer and LMNO(100) top layer (c-direction view).

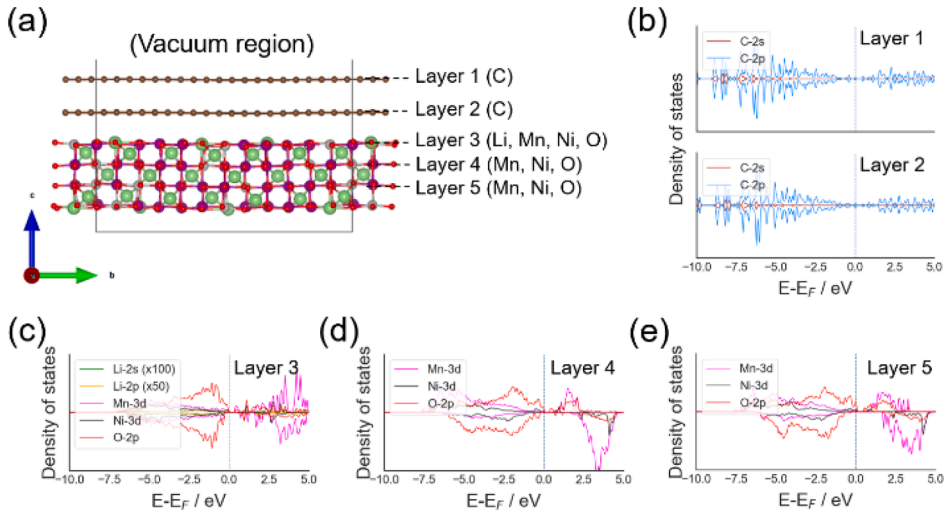

Fig. 7. (a). DFT-optimized lowest-energy LMNO(100)|C(001) interface structure as viewed in the bc-plane. (b-e) Layer-decomposed DFT density of states (DOS) profiles for labeled layers as shown in (7a).

Finally, Table 1 shows a comparison of the electrochemical performance of LFP/C-coated LMNO prepared by different routes in Li-ion batteries. Although direct comparison is difficult due to the slight variation in spinel composition, the LFP/C-coated LMNO composite electrodes show similar initial capacitance values. Among them, the *in-situ* deposition process leads to a high loss of discharge capacity, around ~ 8%, [12] taking pristine LMNO spinel as reference, as a result of possible interfacial reactions during thermal treatment. In contrast, the mechano-fusion and microwave irradiation processes lead to an increase in discharge capacity because of the contribution of iron redox reactions from LFP olivine.

A large amount of olivine (20 wt%) in the LFP/C-coated LMNO prepared by mechano-fusion affects considerably the performance at high C-rates losing more than 40% of the capacity at 10C [11]. In this sense, the low content of olivine (2 wt%), such as that used in the microwave process, provides sufficient chemical stability without affecting the capacity, which remains high even at a high C-rate (105 mAh g^{-1} at 10C). The electrochemical performance at high temperatures (around 60°C), using a similar amount of olivine, shows that LFP/C-coated LMNO obtained by 10-W microwave irradiation leads to notably capacity retention (97%) upon long-term cycling not obtained by other processes so far. The superior performance of the optimized LMNO-LFP/C-10W active material respect to other reported in the literature is associated to the better distribution and adhesion of the LFP/C coating on the LMNO active material conferred by the microwave irradiation technique, which also prevents the occurrence of side reactions during the synthesis procedure avoiding the formation of undesirable or contaminant phases. In addition, thanks to the localized heating, the microwave irradiation technique allows to use smaller amount of the less-conductive LFP/C coating material (2% in the optimized active material) than those used by other synthesis techniques, like mechano-fusion process (20%) [11].

It is anticipated, the use of microwave-assisted synthesis is expected to allow the development of unique materials with synergic properties that cannot be achieved by traditional methods. For instance, this procedure could explore other low-cost spinel compositions and achieve even high capacities with enhanced chemical stability and cyclability at room and high temperatures.

3. Conclusions

The problems associated with the challenging atmospheric conditions required to prepare $LiFePO_4$/C-coated $LiMn_{1.6}Ni_{0.4}O_4$ have been overcome by a simple and fast microwave irradiation process in an organic solvent medium. The preparation of LMNO-LFP/C under mild microwave irradiation conditions (10 W) considerably improves the electrochemical performance of the pristine LMNO spinel, providing not only a high initial discharge capacity, but also high-capacity retention upon long-term cycling and C-rate at 25°C and 60°C, not reported by other processes so far. The improved properties of the electrode are attributed to the high crystallographic order of the LMNO spinel and the improvement of physical adhesion between the LMNO spinel and carbon coating of LFP olivine phase promoted by microwave irradiation, which cannot be obtained by a simple mixture. The application of this procedure is expected to lead to the development of unique materials with synergic properties that cannot be achieved by traditional methods.

Credit Author Statement

F.A. Vásquez: Investigation, original draft preparation, data

Table 1
Electrochemical performance of LFP/C-coated LMNO samples prepared by different routes in Li-ion batteries at 25°C and (55) 60°C.

Route	Temperature, processing time	Discharge capacity (mAh g^{-1})			Capacity retention LMNO-LFP (0.5C)		Ref.
		LFP (wt.%)	LMNO-LFP (0.5C)	LMNO-LFP (10C)	%	Cycle #	
In-situ	550°C, 5 h	1	125 [LOSS OF 8%]	–	95	80	[12]
					*92	*40	
Mechano-fusion	Not specified	20	123 [GAIN OF 7%]	70	82	100	[11]
Microwave	200°C, 7 min	2	119 [GAIN OF 4%]	105	97	100	This work
					80	500	
					*97	*40	

LOSS and GAIN correspond to the discharge capacities loss or gain percentages after the synthesis procedure, taking the capacity of pristine LMNO spinel as a reference in each case.

analysis, **N.C. Rosero-Navarro**: Original draft preparation, editing, conceptualization, data analysis, **R. Jalem**: Conceptualization, DFT analysis, **A. Miura**: Conceptualization, data analysis, editing, **Y. Goto**: Investigation, data analysis, editing. **Y. Tateyama**: Conceptualization, DFT analysis, **J. A. Calderón**: Original draft preparation, editing, conceptualization, data analysis, **K. Tadanaga**: Editing, conceptualization, data analysis.

Funding Sources

Colombian Ministry of Science, Technology and Innovation "Minciencias"; Advanced Graduate School of Chemistry and Materials Science (AGS) and SOUSEI Support Program for Young Researchers in FY2020 of Hokkaido University, Japan Society for the Promotion of Science (JSPS), ALCA-SPRING, HPCI System Research Project.

Declaration of Competing Interest

The authors declare no competing financial interest.

Data availability

Data will be made available on request.

Acknowledgment

F.A. Vásquez and J. Calderón would like to thank Colombian Ministry of Science, Technology and Innovation "Minciencias"; for the financial support provided by the Colombia Scientific Program within the framework of the call Ecosistema Cientıfico (Contract No. FP44842-218- 2018). F.A. Vásquez thanks Minciencias for his doctoral scholarship grant and Advanced Graduate School of Chemistry and Materials Science (AGS) of Hokkaido University by visitor PhD student support (Program 2019). Partial financial support of this work through SOUSEI Support Program for Young Researchers in FY2020 of Hokkaido University to N.C. Rosero-Navarro. SXRD measurement was performed at the beamline BL02B2 of SPring-8 under a proposal No. 2019A1101. R. Jalem and Y. Tateyama thank financial supports by JSPS KAKENHI Grant Numbers JP19H05815 and JP21K14729, by Materials Processing Science project ("Materealize") Grant Number JPMXP0219207397, and by MEXT Grant Number JPMXP1020200301. R. Jalem thanks financial supports by ALCA-SPRING Grant Number JPMJAL1301. The calculations were performed on the supercomputer at NIMS and the supercomputer Fugaku at the RIKEN through the HPCI System Research Project (project ID: hp210105).

Supplementary materials

Supplementary material associated with this article can be found, in the online version, at doi:10.1016/j.apmt.2022.101697.

References

[1] D. Foix, S. Franger, S. Patoux, L. Daniel, D. Gonbeau, Electrode/Electrolyte interface reactivity in high-voltage spinel LiMn1.6Ni0.4O4/Li4Ti5O12 Lithium-Ion BATTERY, J. Phys. Chem. C 114 (2010) 10999–11008.

[2] Y. Ma, Y. Ma, S.L. Dreyer, Q. Wang, K. Wang, D. Goonetilleke, A. Omar, D. Mikhailova, H. Hahn, B. Breitung, T. Brezesinski, High-entropy metal organic frameworks for highly reversible sodium storage, Adv. Mater. 33 (2021), 2101342, https://doi.org/10.1002/adma.202101342.

[3] Z.-Y. Gu, J.-Z. Guo, J.-M. Cao, X.-T. Wang, X.-X. Zhao, X.-Y. Zheng, W.-H. Li, Z.-H. Sun, H.-J. Liang, X.-L. Wu, An advanced high-entropy fluorophosphate cathode for sodium-ion batteries with increased working voltage and energy density, Adv. Mater. (2022), 2110108, https://doi.org/10.1002/adma.202110108.

[4] M.Y. Wang, X.X. Zhao, J.Z. Guo, X.J. Nie, Z.Y. Gu, X. Yang, X.L. Wu, Enhanced electrode kinetics and properties via anionic regulation in polyanionic Na3+xV2(PO4)3−x(P2O7)x cathode material, Green Energy Environ. (2021), https://doi.org/10.1016/j.gee.2020.11.026.

[5] Z.-Y. Gu, J.-Z. Guo, X.-X. Zhao, X.-T. Wang, D. Xie, Z.-H. Sun, C.-D. Zhao, H.-J. Liang, W.-H. Li, X.-L. Wu, High-ionicity fluorophosphate lattice via aliovalent substitution as advanced cathode materials in sodium-ion batteries, InfoMat 3 (2021) 694–704, https://doi.org/10.1002/inf2.12184.

[6] Z.H. Cui, X.F. Lu, J.H. Luo, X. Guo, H.T. Xue, F.L. Tang, Structure stability, electronic property and voltage profile of LiFe1−nNnP1−mMmO4 olivine cathode material, Rare Met 40 (12) (2021) 3512–3519, https://doi.org/10.1007/s12598-020-01689-7.

[7] R. Chen, T. Zhao, X. Zhang, L. Li, F. Wu, Advanced cathode materials for lithium-ion batteries using Nanoarchitectonics, Nanoscale Horizons 1 (2016) 423–444, https://doi.org/10.1039/C6NH00016A.

[8] J. Kim, H. Kim, K. Kang, Surface-modified spinel LiNi0.5Mn1.5O4 for Li-Ion batteries, J. Korean Ceram. Soc. 55 (1) (2018) 21–35, https://doi.org/10.4191/kcers.2018.55.1.08.

[9] Q. Wu, K. Xue, X. Zhang, X. Xie, H. Wang, J. Zhang, Q. Li, Enhanced cyclic stability at elevated temperature of spinel LiNi0.5Mn1.5O4 by Li4Ti5O12 coating as cathode material for high voltage lithium ion batteries, Ceram. Int. 45 (2019) 5072–5079, https://doi.org/10.1016/j.jpowsour.2008.04.091.

[10] J. Chong, J. Zhang, H. Xie, X. Song, G. Liu, V. Battaglia, S. Xun, R. Wang, High Performance LiNi0.5Mn1.5O4 cathode material with a bi-functional coating for lithium Ion Batteries, RSC Adv 6 (23) (2016) 19245–19251, https://doi.org/10.1039/c6ra00119j.

[11] D. Liu, J. Trottier, P. Charest, J. Fréchette, a. Guerfi, a. Mauger, C.M. Julien, K. Zaghib, Effect of Nano LiFePO4 Coating on LiMn1.5Ni0.5O4 5V Cathode for Lithium Ion Batteries, J. Power Sources 204 (2012) 127–132, https://doi.org/10.1016/j.jpowsour.2011.11.059.

[12] W.H. Jang, M.C. Kim, S.H. Kim, V. Aravindan, W.S. Kim, W.S. Yoon, Y.S. Lee, Understanding the exceptional elevated temperature performance of high voltage LiNi0.5Mn1.5O4 Cathodes by LiFePO 4 modification, Electrochim. Acta 137 (2014) 404–410, https://doi.org/10.1016/j.electacta.2014.06.054.

[13] M.-T.F. Rodrigues, G. Babu, H. Gullapalli, K. Kalaga, F.N. Sayed, K. Kato, J. Joyner, P.M. Ajayan, A materials perspective on Li-ion batteries at extreme temperatures, Nat. Energy 2 (8) (2017) 1–14, https://doi.org/10.1038/nenergy.2017.108.

[14] S. Pindar, N. Dhawan, Kinetic evaluation of In-Situ Carbothermic processing of mixed electrode material of discarded Li-Ion batteries, Metall. Mater. Trans. B Process Metall. Mater. Process. Sci. 52 (5) (2021) 3078–3092, https://doi.org/10.1007/s11663-021-02235-1.

[15] A.B. Haruna, P. Mwonga, D. Barrett, C.B. Rodella, R.P. Forbes, A. Venter, Z. Sentsho, P.J. Fletcher, F. Marken, K.I. Ozoemena, Defect-engineered β-MnO2-ΔPrecursors control the structure-property relationships in high-voltage spinel LiMn1.5Ni0.5O4-δ, ACS Omega 6 (39) (2021) 25562–25573, https://doi.org/10.1021/acsomega.1c03656.

[16] S. Hamelet, P. Gibot, M. Casas-Cabanas, D. Bonnin, C.P. Grey, J. Cabana, J. B. Leriche, J. Rodriguez-Carvajal, M. Courty, S. Levasseur, P. Carlach, M. Van Thournout, J.M. Tarascon, C. Masquelier, The effects of moderate thermal treatments under Air on LiFePO 4-Based Nano powders, J. Mater. Chem. 19 (23) (2009) 3979–3991, https://doi.org/10.1039/b901491h.

[17] A.M. Schwenke, S. Hoeppener, U.S. Schubert, Synthesis and modification of carbon nanomaterials utilizing microwave heating, Adv. Mater. 27 (28) (2015) 4113–4141, https://doi.org/10.1002/adma.201500472.

[18] D.F. Stein, R.H. Edgar, M.F. Iskader, D.L. Johnson, S.M. Johnson, C.G. Lob, J. M. Shaw, W.H. Sutton, P.K. Tien, Microwave processing of material: an emerging industrial technology national materials advisory borad commission on engineering and technical systems; Washington (1994).

[19] Rezania, Jafar, H Rahimi, Microwave absorption and its effects on the mechanical and physical properties of carbon fiber and carbon Black/Polypropylene composites, J. Compos. Mater. 16 (2017) 2263–2276, https://doi.org/10.1177/0021998316669578.

[20] J.W. Walkiewicz, G. Kazonich, S.L. McGill, Microwave heating characteristics of selected minerals and compounds, Miner. Metall. Process. 5 (1) (1988) 39–42.

[21] H.C. Su, C.H. Chen, Y.C. Chen, D.J. Yao, H. Chen, Y.C. Chang, T.R. Yew, Improving the adhesion of carbon nanotubes to a substrate using microwave treatment, Carbon N. Y. 48 (3) (2010) 805–812, https://doi.org/10.1016/j.carbon.2009.10.032.

[22] K.T. Butler, G.G. Sai, Pieremanuele Canepa. Designing interfaces in energy materials applications with first-principles calculations, npj Comput. Mater. 5 (19) (2019) 1–2.

[23] Digital MicrographTM. Software by Gatan Inc. *Transmission Electron Microscopy*. Pleasanton.

[24] D.R.G. Mitchell, DiffTools: electron Diffraction Software Tools for DigitalMicrograph™, Microsc. Res. Tech. 71 (2008) 558–593.

[25] Q. Huang, H. Tang, Y. Liu, X.H. Long, P. Liu, X.L. Wang, Q.T. Lei, Q. Deng, Y. Q. Wang, Pore structure evolution of IG-110 graphite during argon ion irradiation at 600 °C, J. Mater. Sci. 54 (8) (2019) 6098–6110, https://doi.org/10.1007/s10853-019-03329-7.

[26] K.R. Chemelewski, E.S. Lee, W. Li, A. Manthiram, Factors Influencing the electrochemical properties of high-voltage spinel cathodes: relative impact of morphology and cation ordering, Chem. Mater. 25 (14) (2013) 2890–2897, https://doi.org/10.1021/cm401496k.

[27] J. Song, D.W. Shin, Y. Lu, C.D. Amos, A. Manthiram, J.B. Goodenough, Role of oxygen vacancies on the performance of Li[Ni0.5–x Mn1.5+x]O4 (X= 0, 0.05, and 0.08) spinel cathodes for Lithium-Ion batteries, Chem. Mater. 24 (2012) 3101–3109, https://doi.org/10.1021/cm301825h.

[28] J. Zheng, J. Xiao, X. Yu, L. Kovarik, M. Gu, F. Omenya, X. Chen, X.-Q. Yang, J. Liu, G.L. Graf, M.S. Whittingham, J.-G. Zhang, Enhanced Li+ Ion transport in

LiNi0.5Mn1.5O4 through control of site disorder, Phys. Chem. Chem. Phys. 14 (2012) 13515–13521, https://doi.org/10.1039/c2cp43007j.
[29] M. Li-wen, C. Bai-zhen, S. Xi-chang, Z. Wen, Y. Xi-yun, Structure and stability of Li-Mn-Ni composite oxides as lithium ion sieve precursors in acidic medium, J. Cent. South Univ. 18 (2011) 314–318, https://doi.org/10.1007/s11771.
[30] J.K. Kim, G. Cheruvally, J.H. Ahn, G.C. Hwang, J.B. Choi, Electrochemical PROPERTIES of Carbon-Coated LiFePO4 synthesized by a modified mechanical activation process, J. Phys. Chem. Solids 69 (10) (2008) 2371–2377, https://doi.org/10.1016/j.jpcs.2008.03.018.
[31] Y. Xie, H. Yu, T. Yi, Y. Zhu, Understanding the thermal and mechanical stabilities of olivine-type LiMPO4 (M =Fe, Mn) as cathode materials for rechargeable lithium batteries from first principles, ACS Appl. Mater. Interfaces 6 (2014) 4033–4042, https://doi.org/10.1021/am4054833.
[32] F.A. Vásquez, N.C. Rosero-Navarro, A. Miura, R. Jalem, Y. Goto, M. Nagao, Y. Tateyama, K. Tadanaga, J.A. Calderón, Kinetic control of the Li0.9Mn1.6Ni0.4O4 spinel structure with enhanced electrochemical performance, Appl. Mater. interfaces (2021), https://doi.org/10.1021/acsami.0c17886.
[33] A.B. Haruna, K.I. Ozoemena, Effects of microwave irradiation on the electrochemical performance of manganese-based cathode materials for lithium-ion batteries, Curr. Opin. Electrochem. 18 (2019) 16–23, https://doi.org/10.1016/j.coelec.2019.08.005.
[34] J.-W. Wena, D.-W. Zhang, Y. Zang, X. Sun, B. Cheng, C.-X. Ding, Y. Yu, C.-H. Chen, One-step synthesis and effect of heat-treatment on the structure and electrochemical properties of LiNi0.5Mn1.5O4 cathode material for lithium-ion batteries, Electrochim. Acta 133 (2014) 515–521, https://doi.org/10.1016/j.electacta.2012.12.069.
[35] Z. Li, Z. Peng, H. Zhang, T. Hu, M. Hu, K. Zhu, X. Wang, [100]-Oriented LiFePO 4 Nanoflakes toward High Rate Li-Ion battery cathode, Nano Lett 16 (2016) 795–799, https://doi.org/10.1021/acs.nanolett.5b04855.
[36] T. Nakamura, H. Gao, K. Ohta, Y. Kimura, Y. Tamenori, K. Nitta, T. Ina, M. Oishi, K. Amezawa, Defect chemical studies on oxygen release from the Li-Rich cathode material Li1.2Mn0.6Ni0.2O2-δ, J. Mater. Chem. A 7 (9) (2019) 5009–5019, https://doi.org/10.1039/c8ta12484a.
[37] J. Kim, A. Huq, M. Chi, N.P.W. Pieczonka, E. Lee, C.A. Bridges, M.M. Tessema, A. Manthiram, K.A. Persson, B.R. Powell, Integrated Nano-domains of disordered and ordered spinel phases in LiNi0.5Mn1.5O4 for Li-Ion batteries, Chem. Mater. 26 (2014) 4377–4386, https://doi.org/10.1021/cm501203r.
[38] S. Hong, S. Mho, I.-H. Yeo, Y. Kang, D.-W. Kim, Structural and electrochemical characteristics of morphology-Controlled Li[Ni0.5Mn1.5]O4 cathodes, Electrochim. Acta 156 (2015) 29–37.
[39] H. Liu, R. Kloepsch, J. Wang, M. Winter, J. Li, Truncated Octahedral LiNi0.5Mn1.5O4 cathode material for ultralong-life lithium-ion battery : positive (100) surfaces in high-voltage spinel system, J. Power Sources 300 (2015) 430–437, https://doi.org/10.1016/j.jpowsour.2015.09.066.
[40] C.R. Birkl, M.R. Roberts, E. McTurk, P.G. Bruce, D.A. Howey, Degradation diagnostics for lithium ion cells, J. Power Sources 341 (2017) 373–386, https://doi.org/10.1016/j.jpowsour.2016.12.011.
[41] T.-F. Yi, J. Mei, Y.-R. Zhu, Key strategies for enhancing the cycling stability and rate capacity of LiNi0.5Mn1.5O4 as high-voltage cathode materials for high power lithium-ion batteries, J. Power Sources 316 (2016) 85–105, https://doi.org/10.1016/j.jpowsour.2016.03.070.
[42] Z. Mao, Y. Sun, K. Scott, Evaluation of apparent lithium-ion diffusion coefficients in FePO4/LiFePO4 cathode material particles from linear non-equilibrium thermodynamics and principle of Electroneutrality, J. Electroanal. Chem. J. 766 (2016) 107–119.
[43] T. Yang, N. Zhang, Y. Lang, K. Sun, Enhanced rate performance of carbon-coated LiNi0.5Mn1.5O4 CATHODE MATERIAL FOR LITHIUM ION BATTeries, Electrochim. Acta 56 (2011) 4058–4064, https://doi.org/10.1016/j.electacta.2010.12.109.